Electrochimica Acta 190 (2016) 588–595

Contents lists available at ScienceDirect

Electrochimica Acta

journal homepage: www.elsevier.com/locate/electacta

# Photochemical Green Synthesis of Nanostructured Cobalt Oxides as Hydrogen Peroxide Redox for Bifunctional Sensing Application

Chia-Yung Su, Wen-Jie Lan, Chieh-Yu Chu, Xiao-Jie Liu, Wei-Yao Kao, Chun-Hu Chen*

*Department of Chemistry, National Sun Yat-sen University, Kaohsiung, 80424, Taiwan*

ARTICLE INFO

*Article history:*
Received 16 November 2015
Accepted 13 December 2015
Available online 17 December 2015

*Keywords:*
Cobalt Oxide
Photochemical synthesis
Hydrogen peroxide
Bifunctional sensing
Nanostructure

ABSTRACT

Photochemically synthesized cobalt oxide hydroxide (PCOH) under UV light has been successfully achieved without the addition of surfactants, templates, or organic solvents at ambient temperatures. PCOH samples can be converted to spinel cobalt oxide (PCO) after the calcination at 500 °C. The *in-situ* growth of hierarchical nanostructures was demonstrated with a three-stage mechanism in the photochemical preparation. The development of nanostructures and elemental condensation under different irradiation time governs the bifunctional-sensing performance of the cobalt oxide products. The formation of nanostructured cobalt oxides involves a free-radical oxidation mechanism in the acidic condition. We further demonstrate that the preparation of sensor-active cobalt oxides under nature sunlight (Solar-2H) is feasible. Compared to the multi-component bifunctional electrocatalysts comprised of enzymes and noble metals, our greenly prepared electrocatalysts, as the single-species sensor, achieve bifunctional hydrogen peroxide detection effectively. The as-produced electrocatalysts utilize electro-oxidative and electro-reductive signals together as bifunctional sensor, maximizing the wide detection range of 0.005–35 mM, a low detection limit of 0.7 μM, selective $H_2O_2$ detection, and ~3000-time higher sensitivity than commercial cobalt oxides.



## 1. Introduction

Solar energy is one of the major resources of clean energy [1,2]. Approaches that harvest sunlight to synthesize useful products, or to convert different forms of energy, are generally considered as green technologies [3–9]. Light-induced preparation has been used in molecular and polymer synthesis for decades, but few examples for generating semiconductor materials (e.g. metal oxides and selenides) are reported [10–13]. The environment of photochemical synthesis is free of high temperature and pressure, advantageous to accomplish controlled synthesis of metastable phases of materials, which provides valuable opportunity for *in-situ* investigation on material growth mechanisms coupled with the characteristic properties [14]. Photochemically generated nanomaterials can be produced with ultrafine sizes, however, they were rarely used in practical applications. This may be attributed to the low production yields and difficulty in product collection caused by fine particle sizes.

Cobalt oxide hydroxide (CoOOH) is a versatile metastable phase and precursor for catalysts, battery, and sensors. In our previous study, the development of nanostructures in CoOOH precursors governs the electrochemical performance of the derived $Co_3O_4$ [15]. Selective synthesis of CoOOH with controllable nanostructures remains challenging using conventional preparation (e.g. hydrothermal, precipitation, etc.) [14,16–20]. Photochemical route as green, clean, and selective approach can be the promising alternative to address the synthetic difficulty.

Hydrogen peroxide is an essential molecule for regulating diverse biological processes, also a side product generated from various enzymatic reactions [21]. Abnormal release of $H_2O_2$ in human bodies is closely related to the diseases of cancers, diabetes, and Alzheimer [21–23]. Besides, many reported biosensors for glucose, cholesterol, lactate, and others are commonly designed on the basis of $H_2O_2$ detection [24,25]. Achievement of highly sensitive and selective detection of $H_2O_2$ is therefore in great demand for general bio-sensing technologies. Bifunctional sensing, by switching modes between $H_2O_2$ electro-oxidation and electro-reduction of one electrocatalyst, creates favorable conditions to maximize linear range of sensors. With one specific mode showing higher sensitivity and/or selectivity than the other one, bifunctional sensing enables the advantage of optimal sensitivity and minimized interference compared to single-mode sensors [26,27]. Bifunctional $H_2O_2$ sensors based on electro-oxidation catalyzed by noble-metals, while electro-reduction is carried out by enzymatic

* Corresponding author.
*E-mail address:* chunhu.chen@mail.nsysu.edu.tw (C.-H. Chen).

http://dx.doi.org/10.1016/j.electacta.2015.12.092
0013-4686/

oxidases, have been reported [27]. Other sensors comprised of transition metal molecules (e.g. ferrocene and vanadium hexacyanoferrate) are capable in mediating both the electro oxidation and reduction of hydrogen peroxide [28,29]. Studies have shown that graphene and metal-nanoparticle composites hybridizing with polymers are also successful transducers for hydrogen peroxide reduction [30,31]. Due to complicated assemblies of composites, and instability of molecules and metals compared to metal oxides, the development of easy-preparation, single-species, low-cost metal oxide catalysts capable of performing bifunctional sensing is desired.

Herein, we demonstrate the photochemical preparation of cobalt oxides with 3D hierarchical nanostructures highly active for bifunctional $H_2O_2$ detection, under both sunlight and ultraviolet. As the green approach in water, there is no need of organic solvents, templates, surfactants, or electricity (sunlight case) in the preparation. The selection of potassium persulfate, owing to its direct photochemical decomposition without any side or intermediate reactions, is for the increase of production yield [32,33]. Both the $H_2O_2$ oxidation and reduction signals of the as-obtained materials can be utilized for quantitative sensing, while these bifunctional signals contribute together for a wide detection range (0.005–35 mM) and low detection limit (0.7 μM).

## 2. Experimental Section

### 2.1. Preparation of photochemically synthesized cobalt oxides

The photochemical procedure was modified from the previous work [13]. Cobalt sulfate heptahydrate (3.6 mmol) and potassium persulfate (3.6 mmol) were mixed in 50 mL of deionized (D.I.) water to produce a pink precursor solution with pH = 5, and then transferred into a quartz tube irradiated with UV light of 256 nm wavelength under stirring in a photoreactor (Panchum PR-200) for 8 hours. The resulting brown precipitates were washed by D.I. water and dried at 60 °C for 12 hours to obtain photochemically synthesized cobalt oxide hydroxides (PCOH-8H). PCOH-8H was subsequently calcined at 500 °C for 6 hours to yield the resultants of $Co_3O_4$, denoted as PCO. The time-dependent experiments were conducted with different reaction time for 1 min, 5 min, 15 min,

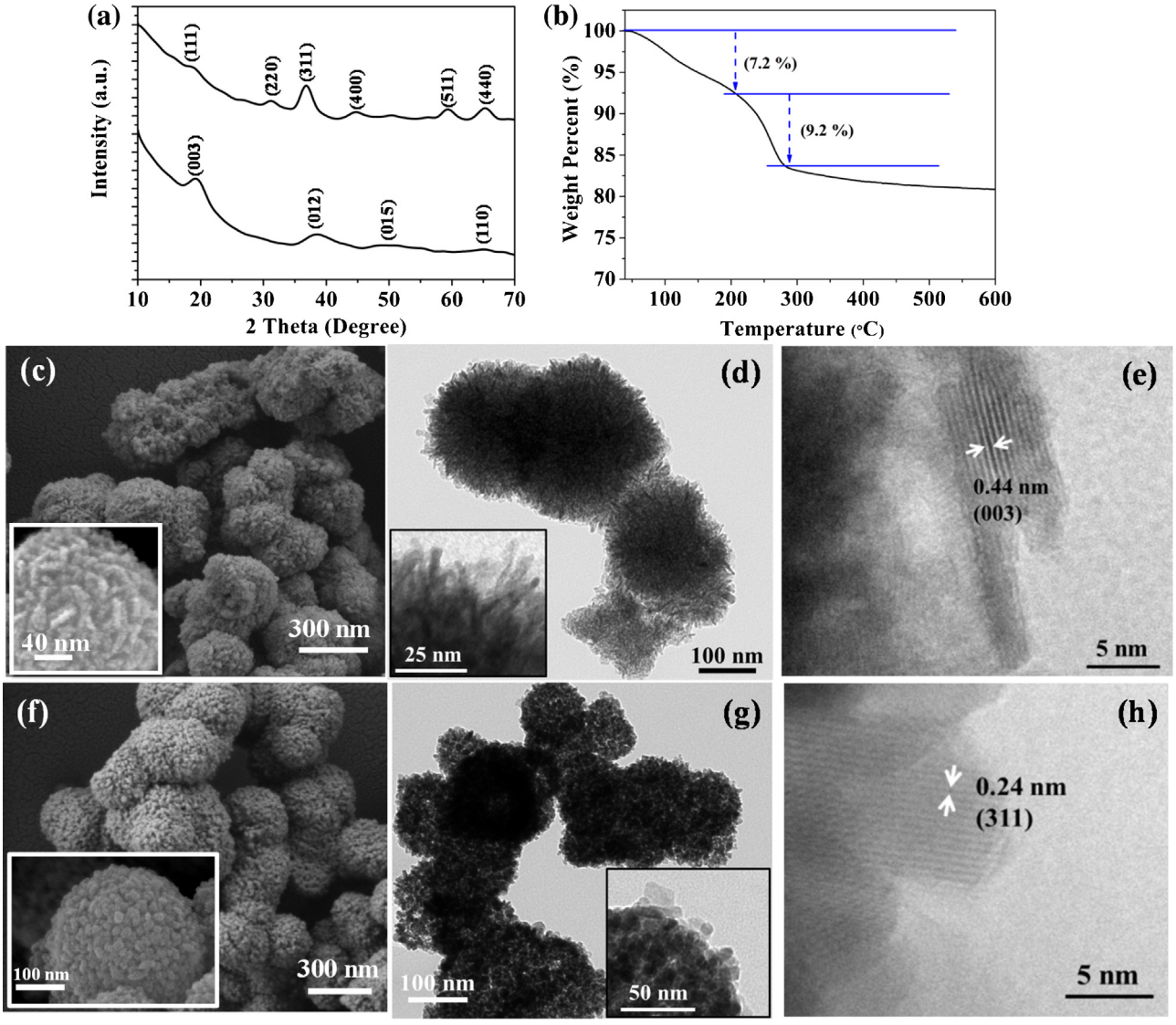


**Fig. 1.** Material characterization of photochemically synthesized cobalt oxide materials. (a) The XRD patterns of PCO-8H (the upper pattern; $Co_3O_4$, JCPDS-9-418) and PCOH-8H (the lower one; CoOOH phase, JCPDS 7-169). (b) The TGA profiles of PCOH-8H. The first 7.2% weight loss ranging from room temperature to 210 °C is due to the desorption of water and physisorbed gas molecules. The SEM (c) and TEM (d) images of PCOH-8H with the corresponding high-magnification insets. (e) The HR-TEM images of nanoflakes in PCOH-8H. The SEM (f) and TEM (g) images of calcined PCO-8H with the corresponding high-magnification insets. (h) The HR-TEM images of PCO-8H.

45 min, 2 hours and 8 hours. Samples prepared by 2-hr and 8-hr UV irradiation are denoted as PCOH-2H and PCOH-8H, respectively. For the samples prepared by sunlight, the pink precursor solution was irradiated by sunlight from 11:00 to 13:00 in days of July at location of 22°30′N 120°14′E. The products after 500 °C calcination were denoted as Solar-2H. For the radical trap experiments, 2,2,6,6-(tetramethylpiperidin-1-yl)-oxy (TEMPO) of 8.12 mmol was added into the precursor solutions of cobalt sulfate heptahydrate and potassium persulfate, which turned the color into orange.

### 2.2. Characterization

Transmission emission microscopy (TEM) images and selected area electron diffraction (SAED) patterns were obtained with a Philliphs CM$^{-}$200 at 200 kV. The morphology of materials was monitored using a Zeiss Supra 55 Gemini field emission scanning electron microscope (FE-SEM) with an acceleration voltage of 1 kV. Thermogravimetry analysis (TGA) was acquired by a PerkinElmer TGA4000 thermal analyzer in $N_2$ from room temperature to 600 °C. The crystalline structure of samples was characterized by using a Bruker D8 advanced X-ray diffraction. The X-ray photoelectron spectroscopy (XPS) data were obtained using a Kratos Axis Ultra DLD with a Mg/Al achromatic source. Cobalt contents of materials were measured with inductively coupled plasma-mass spectroscopy (ICP-MS) analysis on a PE-SCIEX ELAN 6100 DRC. We dissolved 3 mg of samples in a mixture (9 mL) of sulfuric acid and hydrogen peroxide with a ratio of 10 to 1.

### 2.3. Electrochemical measurement

Glassy carbon electrode (GCE) of 3 mm in diameter was polished via 0.3 mm $Al_2O_3$ powders followed by rinsing with D.I. water. For electrochemical experiments, the electrodes were prepared by the following steps. First, the catalyst powder (2 mg) and 1 mL of ethanol were mixed by sonication for 30 min to form a homogeneous suspension. Then 10 μL of the homogeneous suspension was dropped on a GCE and dried at room temperature. Next, 10 μL of Nafion (0.1%) was loaded on top of the dried samples to get the modified electrodes for electrochemical measurements. Electrochemical measurements were all conducted under non-deoxygenated conditions (unless specific description) with a three-electrode configuration using Ag/AgCl (saturate NaCl) and Pt as the reference and counter electrodes, respectively. The material-modified electrodes as working electrodes were used in a CHI614D electrochemical analyzer. Cyclic voltammograms were recorded in potential ranged from -1.0 V to 1.0 V with a scan rate of 50 mV $s^{-1}$. The bifunctional detection was

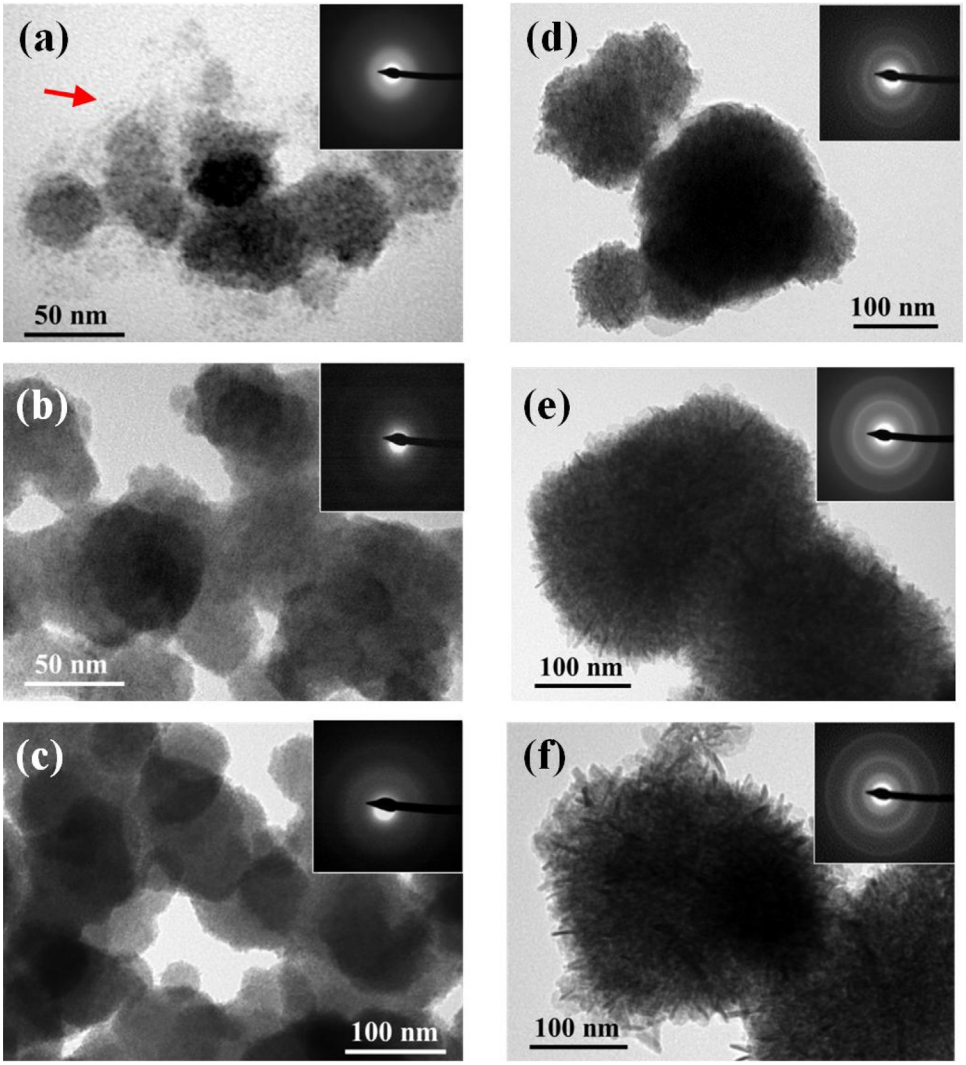


**Fig. 2.** The TEM images and SAED (the insets) of PCOH. A series of PCOH samples with different reaction time before the calcination: (a) 1 min, (b) 5 min, (c) 15 min, (d) 45 min, (e) 2 hr (PCOH-2H), and (f) 8 hr (PCOH-8H).

conducted with a certain volume of hydrogen peroxide solution with various concentrations injected into a 0.1 M phosphate buffer solutions (PBS, pH = 7.2) at potentials of 0.5 V and -0.7 V. For the interference study, the concentration of $H_2O_2$ is 2 mM with the interfering species of 0.1 mM dopamine (DA), acetaminophenol (AP), uric acid (UA), ascorbic acid (AA), and 5 mM glucose. The concentrations of these interfering species were prepared based on the physiological levels [21,34].

## 3. Results and discussion

The photochemically synthesized cobalt oxide hydroxides prepared by 8-hour UV irradiation (PCOH-8H) show the XRD patterns corresponding to layered-structure phase of CoOOH (the lower pattern in Fig. 1a) [13,16]. No impure peaks that belong to phases of spinel $Co_3O_4$ or $Co(OH)_2$ were observed, showing the high selectivity toward CoOOH phase by the photochemical synthesis. As strong oxidants and multi-step procedures are commonly required to selectively produce CoOOH in conventional methods [14–18], our photochemical route with no need of these chemicals rapidly produces pure CoOOH in one step. After the calcination at 500 °C, spinel cobalt oxide (PCO-8H) was obtained using PCOH-8H as the precursor (the upper pattern in Fig. 1a). The second TGA weight loss of 9.2% (210 °C to 280 °C) in Fig. 1b corresponds well to the crystal structure transformation from CoOOH to cubic spinel $Co_3O_4$ [35].

The SEM images (Fig. 1c) of PCOH-8H show the spherical aggregation of flake-like nanoparticles (as shown in the inset) with a diameter of 200-250 nm, much smaller than the similar products prepared by other methods [15]. To describe different levels of the hierarchical structures, material crystal phase is defined as the primary structure, the nanoscaled features/morphologies of particles as the secondary structure, and the assembly behaviors of the particles for the tertiary one. The TEM images of PCOH-8H (Fig. 1d) show the morphology of ultrafine nanoflakes (thickness of 2–3 nm) as the secondary structure [36], different from typical hexagonal morphologies of CoOOH reported in the literature[17]. The lattice fringes (Fig. 1e) of the nanoflakes display a spacing of 0.44 nm, corresponding to $d_{003}$ in the primary structure of CoOOH phase. After the calcination, the nanoflakes were transformed to round shape particles in PCO-8H with the similar aggregation diameters to that before the calcination (Fig. 1f and 1g). The lattice images in PCO (Fig. 1h) reveal a spacing of 0.24 nm, corresponding to $d_{311}$ in the $Co_3O_4$ structure. The XPS spectra confirm the trivalent state of cobalt in PCOH-8H (Fig. S-1). The vanish of satellite peak at 790.8 eV after the calcination demonstrates the mixed-valence states of $Co^{2+}$ and $Co^{3+}$ in PCO-8H[17,37].

### 3.1. Growth process of hierarchical structures

One advantage of photochemical synthesis is able to study the *in-situ* growth procedure of materials in a narrow time domain. The TEM results of time-dependent growth and selected-area electron diffraction (SAED) of a series of PCOH samples are shown in Fig. 2 . After one minute irradiation, the 25-nm tertiary structure assembled by fine, light-contrast particles (< 5 nm of diameter, indicated by the red arrow in Fig. 2a) can rapidly form. The absence of ring patterns in the SAED results shows the amorphous nature at this stage. After the UV exposure for 5 min (Fig. 2b), these fine particles disappear and completely merge into the spherical assembly with the enlarged diameters of 50 nm but still amorphous. Compared to the 5-min samples, the materials obtained after 15-min irradiation exhibit the denser assembly (the darker TEM contrast) with the diameters of tertiary structure ~75 nm and the slightly improved crystallinity (Fig. 2c and the inset). With further proceeding of the photochemical reaction to 45 min, the samples show the even darker contrast and the enlarged diameters around 200 nm (Fig. 2d). The appreciable ring patterns can be observed (the inset of Fig. 2d), demonstrating that the crystallization of CoOOH phase gradually occurs after 45 min of

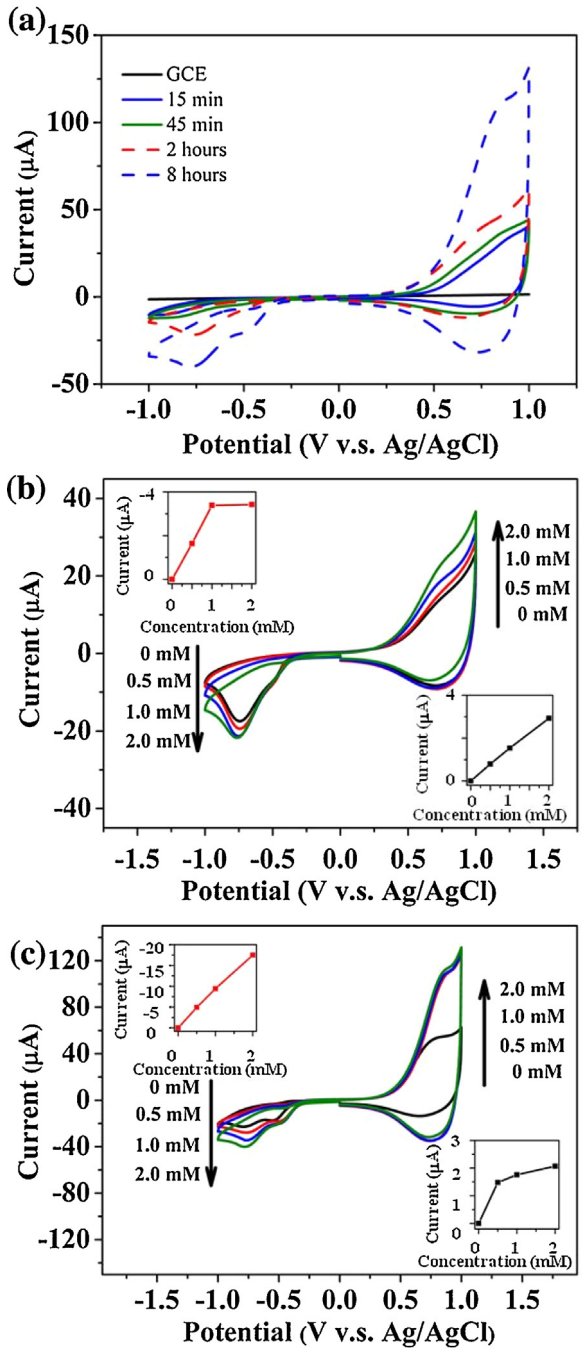


**Fig. 3.** The CVs of PCO modified electrodes with 1 mM hydrogen peroxide in phosphate buffer solution (PBS). (a) The CVs of PCO samples with different photochemical-synthetic time of 15 min (blue line), 45 min (green line), 2 hours (PCO-2H, red dash line), and 8 hours (PCO-8H, blue dash line). (b) The CV results of PCO-2H in the presence of $H_2O_2$ over a concentration range from 0.0 to 2.0 mM at a scan rate of 50 mV $s^{-1}$. The insets represent the corresponding calibration curves based on oxidative signals at 0.5 V (black curve in the right-bottom inset) and reductive signals ones at -0.7 V (red curve in the upper-left inset). (c) The CV results of PCO-8H with different concentrations of $H_2O_2$. The insets show the corresponding calibration curves based on oxidative signals at 0.5 V (black curve in the right-bottom inset) and reductive signals ones at -0.7 V (red curve in the upper-left inset).

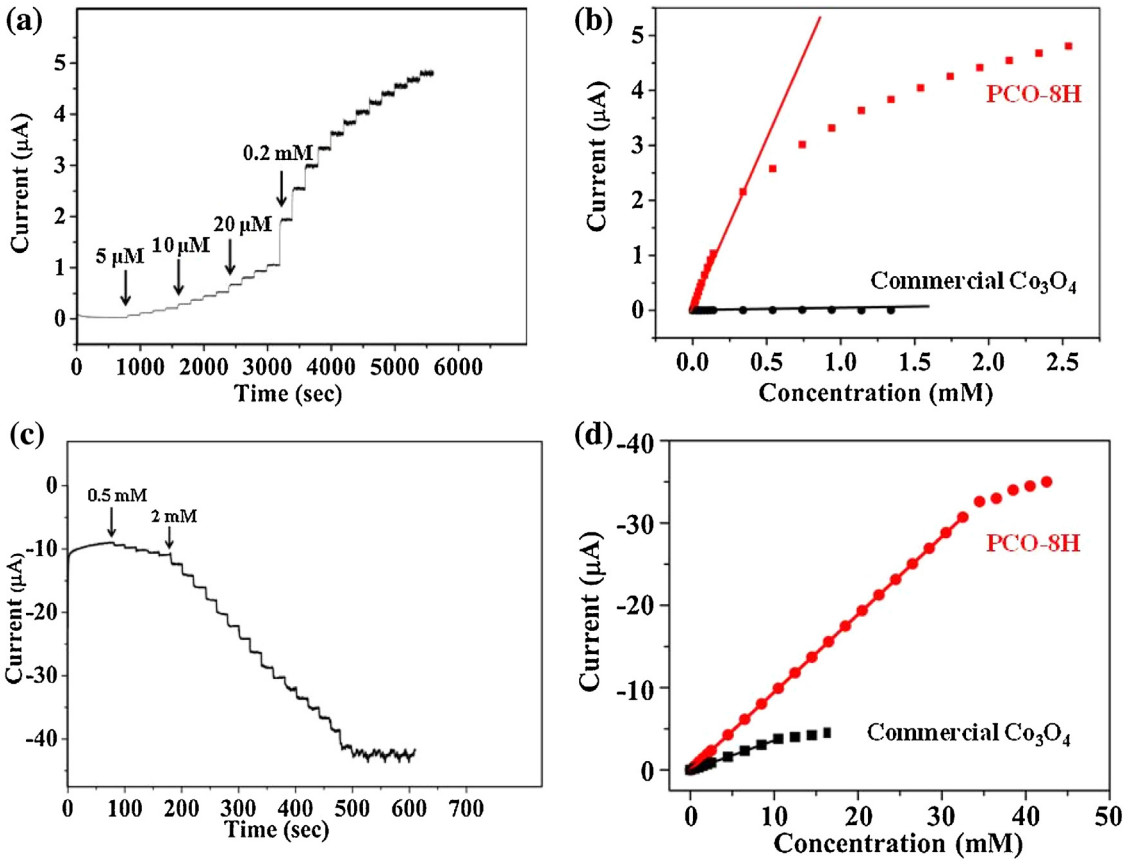


**Fig. 4.** The electrochemical studies of PCO-8H for $H_2O_2$ bifunctional detection. (a) The anodic amperometric responses with the successive injection of $H_2O_2$ at 0.5 V. (b) Comparison of the anodic calibration curves (red line) from (a) with that of commercial $Co_3O_4$ (black line). (c) The cathodic amperometric responses at -0.7 V. (d) The comparison of cathodic calibration curves (red line) from (c) with that of commercial $Co_3O_4$ (black line).

photochemical reaction. After 2-hour synthesis (PCOH-2H), the flake-like features on the surface become clearly visible and crystalline without the significant growth of diameters (Fig. 2e). PCOH-8H shown in Fig. 2f demonstrates the further development of the secondary structure of nanoflakes, rather than the growth of the tertiary structure. These results may indicate that the secondary structure of nanoflake is thermodynamic-favored products, and the controls of nanostructures can be achieved.

### 3.2. Bifunctional sensing of $H_2O_2$

To study the optimal performance of the photochemically synthesized materials for electrochemical sensors, we focused on PCO samples due to their superior activities that come from the mixed-valency nature [15]. The $H_2O_2$ sensing activities of PCO samples significantly depend on the reaction time of photochemical synthesis. The cyclic voltammograms (CVs) in Fig. 3a show that all PCO-modified GCE electrodes exhibit much stronger amperometric signals in both $H_2O_2$ oxidation (anodic currents at 0.5 V) and reduction (cathodic ones at -0.7 V) than bare GCE, clearly demonstrating the electrocatalytic activities of PCO. In general, the samples prepared with the prolonged reaction time result in the increase of both anodic and cathodic currents, capable of performing bifunctional $H_2O_2$ detection [27]. Particularly, the superior reductive currents of PCO-8H (green line) to other PCO materials demonstrate the greatest $H_2O_2$ reduction activities. In addition, we observed the additional reduction peak at -0.45 V in PCO-8H, corresponding to the reduction signal of molecular oxygen (Fig. S-2). This may imply the potential applications of PCO as catalysts for oxygen reduction reaction (ORR) in fuel cells or metal-air battery [38].

The CVs of PCO-2H show the increase of oxidative signals with the higher $H_2O_2$ concentrations (Fig. 3b). The corresponding calibration curves of the insets demonstrate the easy saturation of reduction currents (at 1 mM of $H_2O_2$) than the oxidative ones. Together with the results of Fig. S-2, the reductive signals at 0 mM $H_2O_2$ could be due to the oxygen reduction, as no pre-deoxygenation was conducted. In contrast, for PCO-8H in Fig. 3c, the oxidative signals quickly saturate with 0.5 mM of $H_2O_2$, yet the systematic increase of reduction currents (at -0.7 V) along with the increased concentrations of hydrogen peroxide. The bifunctional sensing behaviors between PCO-2H and PCO-8H show the completely different trends. In addition, the BET surface area measurement shows the nearly identical specific surface areas of these PCO samples (50-54 $m^2/g$). With the minor difference of surface areas, the bifunctional-sensing activities may closely associate with the secondary structures. Serebrennikova and Birss have reported the electrochemical growth of hydrous oxides (e.g. Co and Ni) by injection/expelling of ions [39–41]. The occurrence of this process may also involve the change of the mixed valence of $Co^{3+}/Co^{2+}$ in PCO, potentially contributing to the modulation of sensing activates.

With the greatest amperometric responses of PCO-8H than others, we further evaluated its bifunctional detection performance. Both the oxidative (0.5 V) and reductive (-0.7 V) amperometric responses show the stepwise current increment with the

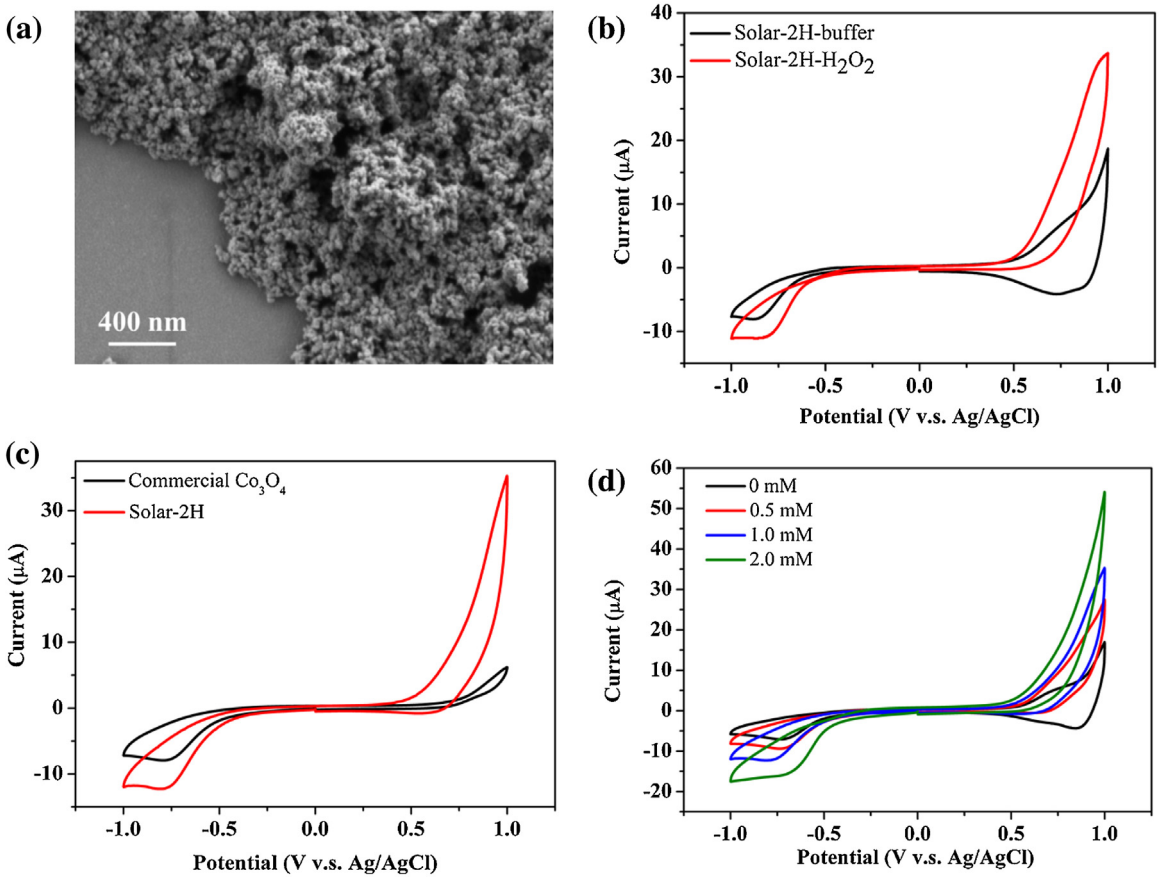


**Fig. 5.** The electrochemical studies of sunlight-synthesized cobalt oxides (Solar-2H). (a) The SEM images of Solar-2H, (b) the CVs of Solar-2H electrodes with and without 1 mM of $H_2O_2$ in PBS, (c) the comparison of commercial cobalt oxides and Solar-2H in the presence of 1 mM $H_2O_2$, and (d) the CV results with various $H_2O_2$ concentrations.

successive step change of $H_2O_2$ concentrations (Fig. 4). The oxidative responses exhibit the amperometric changes at beginning with the addition of 5 μM of $H_2O_2$ (Fig. 4a), but suffering from the current saturation with the later increase of $H_2O_2$ concentrations to around 0.35 mM. The corresponding calibration curve in Fig. 4b reveals the linear range of 0.005 to 0.35 mM ($R^2$ = 0.995) with the high sensitivity of 6.4 μA/mM, ~3380 times greater than commercial $Co_3O_4$ (black line in Fig. 4b). The detection limit of 0.7 μM was obtained with a single-to-noise ratio of 3, even lower than the reported binary cobalt oxides [21]. The cathodic responses at -0.7 V (Fig. 4c) also show the steadily increase with respect to the successive addition of $H_2O_2$. The relatively large detection limit of 6.4 μM (S/N = 3) indicates that the reduction signals are less sensitive compared to the oxidative ones. Fig. 4d demonstrates the calibration curve of cathodic responses with the linear range from 0.25 to 35 mM ($R^2$ = 0.998). The cathodic sensitivity is 0.95 μA/mM (2.7 times greater than commercial $Co_3O_4$), much smaller than that of the anodic one. The comparison of PCO-8H with the reported sensors, based on metal nanoparticles and hybridizing electron-transfer mediators, is summarized in Table S-1. In addition, PCO samples show the high stability and anti-interference capability in the presence of UA, AA, DA, AP and glucose for practical sensor applications (see Fig. S-3).

The combination of bifunctional signals of PCO-8H greatly extends the sensing capability. For example, the $H_2O_2$ oxidation mode has the higher sensitivity and lower detection limit than the reduction one. When the situation is to detect highly diluted

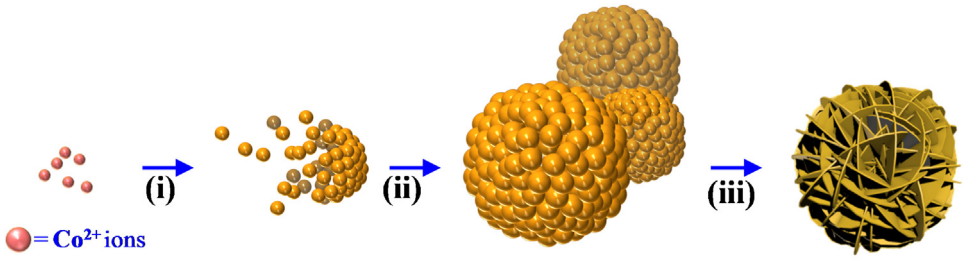


**Scheme 1.** The illustration of nanostructure development of PCOH materials by the photochemical synthesis. The first stage (i) represents the rapid formation of ultrafine particles (yellow dots) from aqueous cobalt ions (pink dots), and these ultra-fine particles merge into the spherical aggregations. The second stage (ii) shows the growth of both fine particles and aggregations. In the final stage (iii), the structural reorganization occurs via the transformation of smooth surface into 3D nanoflake structure.

concentrations of hydrogen peroxide (micromolar scale), one should use oxidation signals. On the other hand, the reduction mode is a more suitable choice if the detection concentrations are in a range of tens of millimolar. The linear range of $H_2O_2$ oxidation is 0.005 to 0.35 mM, while that for reduction signals is 0.25–35 mM. These two ranges overlap in 0.25–0.35 mM, suggesting that the theoretically quantitative analysis can be extended ranging from 0.005 to 35 mM by switching between the two modes. Such the wide detection range of single-component PCO-8H is greater than the reported multi-component composites [26,27,42–44].

### 3.3. Green synthesis of PCO by solar energy

Based on the success of UV-assisted photochemical synthesis, we attempted to utilize sunlight as a green energy source to produce PCO electrocatalysts. For the uniform light flux and controlled temperatures under sunlight, the synthesis was conducted under the sunlight irradiation for 2 hours rather than 8 hours. The mixture of precursor solution was placed under sunlight for two hours (11:00 to 13:00 of days in July). The as-produced samples (Solar-2H) show the spherical morphology (Fig. 5a) with the relatively smaller diameters (~ 50 nm) compared to that of PCO-2H. Solar-2H exhibits the similar capability for bifunctional detection in the presence of $H_2O_2$ (Fig. 5b), where both the anodic and cathodic currents are higher than the blank conditions. Solar-2H also displays the higher activities than commercial $Co_3O_4$ (Fig. 5c). The cathodic and anodic signals of Solar-2H are enlarged as the increased concentrations of $H_2O_2$ (0–2 mM), showing a similar sensing activity to PCO samples (Fig. 5d). The significant increase of the anodic currents of Solar-2H with a typical catalytic shape of the CV clearly indicates the catalytic oxidation of $H_2O_2$. This direct synthesis of nanomaterials solely using solar energy reveals the new concepts for green synthesis of high-performance electrocatalysts.

### 3.4. Material formation of photochemical synthesis

To study the formation mechanism of this process, we added a radical trap reagent (TEMPO) in the reaction mixture for the photochemical synthesis. The resultant mixture exhibits the orange color and no material formation after UV irradiation for 8 hours (Fig. S-4), indicating that PCOH formation depends on free radical mechanism. In the presence of radical trap reagent, TEMPO consumes the photo-generated radicals of $SO_4^{\bullet -}$ and thus hinders the formation of PCOH. This is different from the reported study showing that photochemical synthetic CoOOH needs the presence of Co-halide bonds [14]. The formation processes may go through the ultraviolet photolysis of aqueous persulfate ions to yield highly oxidative $SO_4^{\bullet -}$ as the following equation [33]:

$$2Co^{2+}(aq) + 2SO_4^{\bullet -}(aq) \rightarrow 2CoOOH(s) + 2SO_4^{2-}(aq) + 6H^+(aq) \quad (1)$$

Although the detailed correlation between bifunctional sensing activities and hierarchical nanostructures remains unclear, the results indicate growth mechanism of the secondary structures may play the key roles. As shown in Scheme 1, the material growth begins with the first stage of generating amorphous, metastable products without a stoichiometry for specific phases. In the second stage, roughly ranging from 15 min to 2 hours, elemental condensation and crystallization may gradually occur with the tertiary structure enlargement. Finally, the development of the extrusive nanoflakes may lead to the high degree of catalytic surface exposure. Furthermore, the phase transformation of the well-crystallized secondary structure may yield the electro-catalytic-active defects and/or vacancies, beneficial for the enhanced catalytic performance [45].

## 4. Conclusion

Photochemical synthesis has been successfully demonstrated as an effective and green route to produce bifunctional electrocatalysts of cobalt oxides with a wide detection range (0.005–35 mM). The bifunctional-sensing performance highly depends on development of the secondary structures. Controlled synthesis of specific metastable phase, nanostructures, and complex composites by photochemical routes may be amiable for the future design of new electrocatalysts. Further extension of this free radical-mediated photochemical preparation for diverse nanomaterials is actively pursuing.

## Acknowledgement

We thank the funding from Ministry of Science and Technology, Taiwan (R.O.C.) under Grant No. MOST103-2113-M-110-002-MY2.

## Appendix A. Supplementary data

Supplementary data associated with this article can be found, in the online version, at http://dx.doi.org/10.1016/j.electacta.2015.12.092.

## References

[1] S. Chu, A. Majumdar, Opportunities and challenges for a sustainable energy future, Nature 488 (2012) 294–303.
[2] S.Y. Reece, J.A. Hamel, K. Sung, T.D. Jarvi, A.J. Esswein, J.J. Pijpers, et al., Wireless solar water splitting using silicon-based semiconductors and earth-abundant catalysts, Science 334 (2011) 645–648.
[3] M. Gao, W. Sheng, Z. Zhuang, Q. Fang, S. Gu, J. Jiang, et al., Efficient water oxidation using nanostructured alpha-nickel-hydroxide as an electrocatalyst, J Am Chem Soc 136 (2014) 7077–7084.
[4] J.E. Coughlin, Z.B. Henson, G.C. Welch, G.C. Bazan, Design and Synthesis of molecular donors for solution-processed high-efficiency organic solar cells, Acc. Chem. Res. 47 (2014) 257–270.
[5] H. Zhou, Q. Chen, G. Li, S. Luo, T.-b. Song, H.-S. Duan, et al., Interface engineering of highly efficient perovskite solar cells, Science 345 (2014) 542–546.
[6] L. Xu, Y.-L. Hu, C. Pelligra, C.-H. Chen, L. Jin, H. Huang, et al., ZnO with different morphologies synthesized by solvothermal methods for enhanced photocatalytic activity, Chem. Mater. 21 (2009) 2875–2885.
[7] Y. Zhou, M. Yang, A.L. Vasiliev, H.F. Garces, Y. Zhao, D. Wang, et al., Growth control of compact $CH_3NH_3PbI_3$ thin films via enhanced solid-state precursor reaction for efficient planar perovskite solar cells, J. Mater. Chem. A 3 (2015) 9249–9256.
[8] A.L. Linsebigler, G. Lu, J.T. Yates, Photocatalysis on $TiO_2$ surfaces: principles, mechanisms, and selected results, Chem. Rev. 95 (1995) 735–758.
[9] C.C. Chou, F.C. Hu, H.H. Yeh, H.P. Wu, Y. Chi, J.N. Clifford, et al., Highly efficient dye-sensitized solar cells based on panchromatic ruthenium sensitizers with quinolinylbipyridine anchors, Angew. Chem. Int. Ed. 53 (2014) 178–183.
[10] D.H. Webber, R.L. Brutchey, Photolytic preparation of tellurium nanorods, Chem. Commun (2009) 5701–5703.
[11] D.H. Webber, R.L. Brutchey, Photochemical synthesis of bismuth selenide nanocrystals in an aqueous micellar solution, Inorg. Chem. 50 (2011) 723–725.
[12] L. Balan, C. Matei Ghimbeu, L. Vidal, C. Vix-Guterl, Photoassisted synthesis of manganese oxide nanostructures using visible light at room temperature, Green Chem 15 (2013) 2191–2199.
[13] C.K. King'ondu, A. Iyer, E.C. Njagi, N. Opembe, H. Genuino, H. Huang, et al., Light-assisted synthesis of metal oxide hierarchical structures and their catalytic applications, J. Am. Chem. Soc. 133 (2011) 4186–4189.
[14] S.R. Alvarado, Y. Guo, T.P.A. Ruberu, A. Bakac, J. Vela, Photochemical versus thermal synthesis of cobalt oxyhydroxide nanocrystals, J. Phys. Chem. C 116 (2012) 10382–10389.
[15] W.-J. Lan, C.-C. Kuo, C.-H. Chen, Hierarchical nanostructures with unique Y-shaped interconnection networks in manganese substituted cobalt oxides: the enhancement effect on electrochemical sensing performance, Chem. Commun. 49 (2013) 3025–3027.
[16] C.-H. Chen, S.F. Abbas, A. Morey, S. Sithambaram, L.-P. Xu, H.F. Garces, et al., Controlled Synthesis of Self-assembled metal oxide hollow spheres via tuning redox potentials: versatile nanostructured cobalt oxides, Adv. Mater. 20 (2008) 1205–1209.
[17] J. Yang, H. Liu, W.N. Martens, R.L. Frost, Synthesis and characterization of cobalt hydroxide, cobalt oxyhydroxide, and cobalt oxide nanodiscs, J. Phys. Chem. C 114 (2010) 111–119.

[18] E. Hosono, S. Fujihara, I. Honma, M. Ichihara, H. Zhou, Synthesis of the CoOOH fine nanoflake film with the high rate capacitance property, J. Power. Sources 158 (2006) 779–783.
[19] Y. Ding, L. Xu, C. Chen, X. Shen, S.L. Suib, Syntheses of nanostructures of cobalt hydrotalcite like compounds and $Co_3O_4$ via a microwave-assisted reflux method, J. Phys. Chem. B 112 (2008) 8177–8183.
[20] F. Li, J. Chen, Q. Zhang, Y. Wang, Hydrous ruthenium oxide supported on $Co_3O_4$ as efficient catalyst for aerobic oxidation of amines, Green Chem. 10 (2008) 553–562.
[21] C.-C. Kuo, W.-J. Lan, C.-H. Chen, Redox preparation of mixed-valence cobalt manganese oxide nanostructured materials: highly efficient noble metal-free electrocatalysts for sensing hydrogen peroxide, Nanoscale 6 (2014) 334–341.
[22] B.C. Dickinson, C.J. Chang, A targetable fluorescent probe for imaging hydrogen peroxide in the mitochondria of living cells, J. Am. Chem. Soc. 130 (2008) 9638–9639.
[23] M. Spanos, J. Gras-Najjar, J.M. Letchworth, A.L. Sanford, J.V. Toups, L.A. Sombers, Quantitation of hydrogen peroxide fluctuations and their modulation of dopamine dynamics in the rat dorsal striatum using fast-scan cyclic voltammetry, ACS Chem. Neurosci. 4 (2013) 782–789.
[24] W. Chen, S. Cai, Q.Q. Ren, W. Wen, Y.D. Zhao, Recent advances in electrochemical sensing for hydrogen peroxide: a review, Analyst 137 (2012) 49–58.
[25] X. Jia, G. Hu, F. Nitze, H.R. Barzegar, T. Sharifi, C.W. Tai, et al., Synthesis of palladium/helical carbon nanofiber hybrid nanostructures and their application for hydrogen peroxide and glucose detection, ACS Appl. Mater. Interfaces 5 (2013) 12017–12022.
[26] E.M.I.M. Ekanayake, D.M.G. Preethichandra, K. Kaneto, Bi-functional amperometric biosensor for low concentration hydrogen peroxide measurements using polypyrrole immobilizing matrix, Sens. Actuator B-Chem. 132 (2008) 166–171.
[27] S. Gamburzev, P. Atanasov, A.L. Ghindilis, E. Wilkins, A. Kaisheva, I. Iliev, Bifunctional hydrogen peroxide electrode as an amperometric transducer for biosensors, Sens. Actuator B-Chem. 43 (1997) 70–77.
[28] N. Sun, L. Guan, Z. Shi, N. Li, Z. Gu, Z. Zhu, et al., Ferrocene peapod modified electrodes: preparation, characterization, and mediation of $H_2O_2$, Anal. Chem, 7 8 (2006) 6050–6057.
[29] C.G. Tsiafoulis, P.N. Trikalitis, M.I. Prodromidis, synthesis, characterization and performance of vanadium hexacyanoferrate as electrocatalyst of $H_2O_2$, Electrochem. Commun. 7 (2005) 1398–13404.
[30] A. Michopoulos, A. Kouloumpis, D. Gournis, M.I. Prodromidis, Performance of layer-by-layer deposited low dimensional building blocks of graphene-prussian blue onto graphite screen-printed electrodes as sensors for hydrogen peroxide, Electrochim. Acta 146 (2014) 477–484.
[31] V.A. Gatselou, D.L. Giokas, A.G. Vlessidis, M.I. Prodromidis, Rhodium nanoparticle-modified screen-printed graphite electrodes for the determination of hydrogen peroxide in tea extracts in the presence of oxygen, Talanta 134 (2015) 482–487.
[32] J.L.R. Morgan, R.H. Crist, The photochemical decomposition of potassium persulfate. I, J. Am. Chem. Soc. 49 (1927) 16–25.
[33] J.L.R. Morgan, R.H. Crist, The photochemical decomposition of potassium persulfate. I, J. Am. Chem. Soc. 49 (1927) 338–346.
[34] X. Qin, W. Lu, Y. Luo, G. Chang, A.M. Asiri, A.O. Al-Youbi, et al., Green photocatalytic synthesis of Ag nanoparticle-decorated $TiO_2$ nanowires for nonenzymatic amperometric $H_2O_2$ detection, Electrochim. Acta 74 (2012) 275–279.
[35] Z.P. Xu, H.C. Zeng, Thermal evolution of cobalt hydroxides: a comparative study of their various structural phases, J. Mater. Chem. 8 (1998) 2499–2506.
[36] J. Yang, T. Sasaki, Synthesis of CoOOH hierarchically hollow spheres by nanorod self-assembly through bubble templating, Chem. Mater. 20 (2008) 2049–2056.
[37] J.C. Carver, G.K. Schweitzer, Use of X-ray photoelectron spectroscopy to study bonding in Cr, Mn, Fe, and Co compounds, J. Chem. Phys. 57 (1972) 973.
[38] Y. Ma, H. Wang, J. Key, V. Linkov, S. Ji, X. Mao, et al., Ultrafine iron oxide nanoparticles supported on N-doped carbon black as an oxygen reduction reaction catalyst, Int. J. Hydrogen Energy 39 (2014) 14777–14782.
[39] I. Serebrennikova, V.I. Birssi, Structural and compositional properties of sol-gel formed Ni, Co and Ni-Co oxide film, J. Mater. Sci. 36 (2001) 4331–4343.
[40] I. Serebrennikova, V.I. Birss, Mass changes accompanying the electrochemical reaction of sol-gel formed 50:50 Ni–Co oxide films, J. Electroanal. Chem. 493 (2000) 108–116.
[41] I. Serebrennikova, V.I. Birss, Electrochemical behavior of sol-gel produced Ni and Ni-Co oxide films, J. Electrochem. Soc. 144 (1997) 566–572.
[42] L. Qian, X. Yang, Composite film of carbon nanotubes and chitosan for preparation of amperometric hydrogen peroxide biosensor, Talanta 68 (2006) 721–727.
[43] W. Yang, Y. Li, Y. Bai, C. Sun, Hydrogen peroxide biosensor based on myoglobin/colloidal gold nanoparticles immobilized on glassy carbon electrode by a Nafion film, Sens. Actuator B-Chem. 115 (2006) 42–48.
[44] M. Ammam, E.B. Easton, Novel organic–inorganic hybrid material based on tris (2,2′-bipyridyl) dichlororuthenium(II) hexahydrate and dawson-type tungstophosphate $K_7[H_4PW_{18}O_{62}]\cdot 18H_2O$ as a bifuctional hydrogen peroxide electrocatalyst for biosensors, S Sens. Actuator B-Chem. 161 (2012) 520–527.
[45] S. He, C. Li, H. Chen, D. Su, B. Zhang, X. Cao, et al., A surface defect-promoted Ni nanocatalyst with simultaneously enhanced activity and stability, Chem. Mater. 25 (2013) 1040–1046.